Acta Materialia 166 (2019) 67–74

Contents lists available at ScienceDirect

Acta Materialia

journal homepage: www.elsevier.com/locate/actamat

Full length article

Grain boundary structure and migration in graphene *via* the displacement shift complete lattice

Emil Annevelink*, Elif Ertekin, Harley T. Johnson

Department of Mechanical Science and Engineering, University of Illinois at Urbana-Champaign, Urbana, IL, 61801, USA

ARTICLE INFO

Article history:
Received 6 August 2018
Received in revised form
7 December 2018
Accepted 13 December 2018
Available online 17 December 2018

Keywords:
Graphene
Grain boundary
Displacement shift complete lattice
Dislocation

ABSTRACT

We describe grain boundary structure and migration in graphene using the concept of dislocations in the displacement shift complete lattice. The equivalence of displacement shift complete lattice dislocations and grain boundary kinks in graphene is shown both topologically and energetically. Topologically, a grain boundary kink and a displacement shift complete lattice dislocation both translate the coincident site lattice. The energetic equivalence is established through comparison of atomistic and continuum elasticity models of metastable states to show that DSC dislocations are well-described by elasticity theory. The continuum results are fitted to the atomistic results with one adjustable parameter, the DSC dislocation core radius. The atomistic results reveal that low sigma boundaries have large energy barriers to grain boundary motion, which match continuum results obtained for smaller core radii dislocations. The larger energy barriers for low sigma boundaries are consistent with experimental results reporting isolated, low sigma boundaries in grown graphene. The trends in the dislocation Burgers vector and fitted core radii across grain boundaries of different misorientation are expressed in a unified model. The analysis provides a framework for understanding grain boundary motion in graphene and can serve as a basis for engineering the atomic structure of graphene.

1. Introduction

Graphene, the most extensively studied member of the class of two-dimensional materials, offers new device possibilities in electronics [1–3], chemical processing [4,5], and biological sensing [6,7]. In order to harness the properties of graphene in engineering devices, it is necessary to have precise control over the atomic structure that arises during synthesis, including the structure and distribution of grain boundaries and the resulting grain size. Common growth techniques such as chemical vapor deposition result in synthesized samples of variable crystallinity, grain size, and grain boundary distribution [8,9]. The uncontrolled structure of grain boundaries results in a large variation of properties. For example, the fracture strength varies by a factor of three [10] and the electronic conductivity can vary by an order of magnitude [11] based on the grain boundary distribution. On the other hand, if control over the grain structure could be achieved, several possibilities open up such as tailoring the atomic structure to achieve desired electronic and mechanical properties.

Although grain boundary structure has been identified as a candidate approach for controlling properties, the complexity of the structure and migration mechanisms of grain boundaries has thus far hindered progress. Grain boundaries are regions of atomic reconstruction between two neighboring, misaligned grains. As in conventional three-dimensional materials, grain boundaries in graphene tend to be composed of periodically arranged edge dislocations – here pairs of rings with 5 and 7 atoms [12]. The edge dislocations that comprise a grain boundary can be arranged in differing orientations with variable spacing. These degrees of freedom alter the symmetries of grain boundaries and produce an extensive configurational phase space. Statistical and Fourier analysis of atomic scale microscopy images has shown that grain boundaries tend to prefer misorientation angles around $\theta = 30^\circ$ [8,9]. However, there is little explanation for the particular atomic arrangements that produce the misorientation angles.

Several recent efforts have made progress in analyzing the formation mechanisms and extensive configuration space of grain boundaries in graphene. To understand formation mechanisms, Zhuang et al. used kinetic Monte Carlo to evolve amorphous 2D carbon into graphene using bond rotations [13]. They identified two regimes: first, the coalescence of edge dislocations to form grain

---

* Corresponding author.
E-mail address: annevel2@illinois.edu (E. Annevelink).

https://doi.org/10.1016/j.actamat.2018.12.030
1359-6454/

boundaries and, next, the modification of the atomic scale grain boundary structure during annealing. This process yields misorientation angles around $\theta = 30^\circ$. This corresponds to experimental observations that show the formation of a variety of grain boundary angles which anneal into structures with $\theta = 30^\circ$ [9]. Shekhawat et al. mapped the phase space of symmetric grain boundaries similar to those that form in the first stage of Zhuang et al. Here, symmetric refers to a grain boundary whose direction bisects the misorientation angle *i.e.* a line angle θ_l E = 0. Their results reveal the existence of special misorientation angles corresponding to low-energy 'cusps' in the relation between the grain boundary line energy and θ [14]. The predicted cusps at $\theta = 32.2^\circ$ and $\theta = 21.78^\circ$ correspond to the misorientation angles commonly observed in both simulation and experiment, although the specific atomic scale structures vary.

In contrast to the symmetric structures predicted from simulation, experimental observations also show the presence of high dislocation density grain boundaries whose origins are not clear [8]. Such higher dislocation density grain boundaries may form, for example, when two symmetric, low-energy grain boundaries merge (the annealing stage of Zhuang et al.). Therefore, in addition to the thermodynamic study of the line energy of pristine grain boundaries, it is of interest to consider the kinetic grain boundary migration mechanisms across a wide set of grain boundary angles. This is of interest not only for misorientations θ that are observed in experiment, but also for grain boundaries with misorientation angles θ that may have disappeared during subsequent processing or annealing.

In this work, we present a topological framework to describe the conservative migration mechanisms of grain boundaries and assess their mobility for different misorientations θ. In this framework, grain boundary motion occurs *via* the formation and propagation of kinks in the grain boundary [15,16] as shown in Fig. 1. For example, the symmetric grain boundaries shown in Fig. 1a and b move when edge dislocations glide with respect to a grain boundary resulting in the formation of a kink of length K as shown in Fig. 1c and d. Subsequent glide of adjacent dislocations results in the propagation of the kink walls and extension of K until the entire grain boundary has shifted. The energy barrier for this process is considered to represent the energy barrier for the conservative motion of the grain boundary, where non-conservative motion, through pure step motion, for example—that depends on chemical potential minimization—is ignored. As for the case of bulk copper and other three dimensional materials [17], we show that in graphene a double kink in a grain boundary is equivalent to a dislocation dipole in the *displacement shift complete* (DSC) lattice [18]. We develop a continuum approach, containing only one adjustable parameter, to predict the energetics of kinked grain boundaries and determine migration barriers. The continuum description is shown to reproduce atomistic simulations of grain boundary motion (kink formation and propagation) and trends in the migration barrier for different misorentiations θ. Our results suggest that the prevalence of $\theta = 32.2^\circ$ and $\theta = 21.78^\circ$ boundaries commonly observed in experiments may arise from their relatively large energy barriers for motion. Similarly, low angle boundaries have low migration barriers, indicating that they may more readily anneal out of the system.

2. Grain boundaries, kinks and their relation to the displacement shift complete lattice

To construct atomic scale models of grain boundaries with arbitrary misorientation θ, we use a modified version of the approach developed by Shekhawat et al. [14]. A unit cell containing two grain boundaries of opposite orientation with the smallest repeat height is first generated. The minimum unit cell height is equivalent to the coincident site lattice (CSL) spacing, a_{CSL}, of two lattices misoriented by θ. Each grain boundary in the unit cell

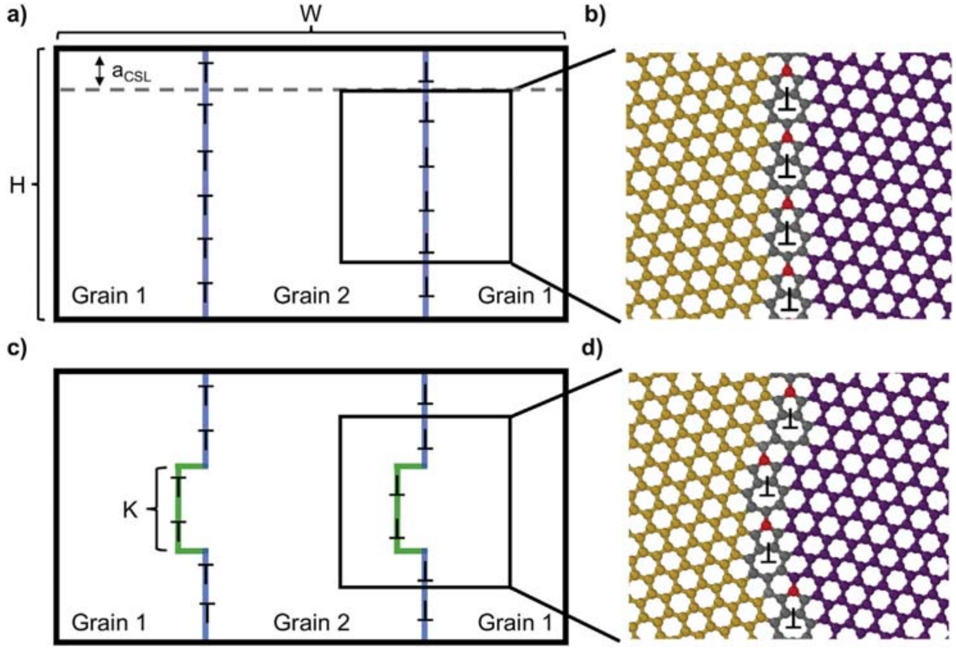

Fig. 1. (a,b) Straight and (c,d) kinked grain boundaries in graphene. In (a,c), periodic supercells of height H and width W containing a pair of anti-parallel grain boundaries are shown. The gray dashed line in (a) marks the smallest unit cell height of a grain boundary given by a_{CSL}. In (c) a portion of the grain boundary (K units long) has migrated, corresponding to the formation of a double kink. In (b,d), the corresponding atomic-scale structure for a $\Sigma 7$ boundary are shown. The different grain orientations are shown by gold/purple coloring, while the grain boundaries are gray. The migration of the grain boundary corresponds to a shift in the coincident site lattice (CSL) (red points) in the region where the migration has occurred. (For interpretation of the references to color in this figure legend, the reader is referred to the Web version of this article.)

contains one or two edge dislocations depending on the type of grain boundary (*e.g.* zig-zag or armchair) [10]. An example of a unit cell is seen in Fig. 1a. The unit cells are stacked vertically to generate supercells of height H and width W, where the grain boundaries are $W/2$ apart. To indicate supercell sizes, we use dimensionless parameters $\overline{H} = H/a_{CSL}$ and $\overline{K} = K/a_{CSL}$, which represent the supercell and kink height in terms of the number of repeat units. For instance, Fig. 1a shows a supercell built by stacking six unit cells ($\overline{H} = 6$) with $\overline{K} = 0$, while Fig. 1b shows the same supercell ($\overline{H} = 6$) but with $\overline{K} = 2$. Fig. 1b,d shows the atomistic representations for the associated $\theta = 21.78^\circ$ grain boundary.

Here onwards, we classify each grain boundary according to its sigma number Σ, which exhibits a one to one relationship with the misorientation angle θ and is closely related to the concept of the CSL [19]. For a given grain boundary as shown in Fig. 2a, the CSL is defined as the set of lattice points of Lattice 1 (gold points) that, if extended across the grain boundary, would coincide exactly with the points of Lattice 2 (purple points), and *vice versa*. The CSL for the grain boundary in Fig. 2a is shown in red. The Σ number then relates the CSL to the real graphene lattice through the relation $\Sigma = A_{CSL}/A_{lat}$, where A_{CSL} and A_{lat} are the areas of the primitive unit cells of the CSL and graphene respectively. The areas, A_{CSL} and A_{lat}, can be found from Fig. 2a to find Σ for the $\theta = 21.78^\circ$ boundary to be 7. Alternatively, numerical routines have been developed that only use θ to find Σ [20].

Grain boundary motion occurs by nucleating double kinks in symmetric grain boundaries and propagating the kinks so that they are a distance $\overline{K}$ apart, as shown in Fig. 1c and d. In the atomistic picture, kinks nucleate through the glide of an edge dislocation. The kink propagates by sequentially gliding adjacent edge dislocations, causing the grain boundary to shift and thereby the location of registry between the grains, the CSL points, to shift. As adjacent dislocations in the grain boundary glide, $\overline{K}$ increases to become equal to $\overline{H}$ at which point the grain boundary has migrated by one dislocation Burgers vector. The shift of the CSL points is seen in Fig. 1b,d, where the glide of an edge dislocation moves the CSL (colored in red) by one dislocation Burgers vector. The shift in the CSL points can also be seen in Fig. 2b in the region where the grain boundary edge dislocations have moved (the region between the gray lines).

By associating the motion of CSL points with grain boundary motion, we can formalize the DSC interpretation of grain boundary motion. The DSC lattice, shown in Fig. 2 in cyan, is the sparsest lattice that includes all points of crystal Lattices 1 and 2 on both sides of the grain boundary. A feature of the DSC lattice is that it enumerates the set of allowable shifts that maintain a given CSL. As Fig. 2b shows, even though Lattices 1 and 2 and the CSL are shifted between the gray lines, all points of all lattices, even in the shifted region, are captured by the DSC lattice.

The utility of the DSC lattice is that it enumerates shifts that correspond to all possible kinks in a given grain boundary. Fig. 2b shows the equivalence of the grain boundary kink in Fig. 1d and a dislocation in the DSC lattice. The blue and green lines in Fig. 2b show the kink structure that is formed in Fig. 1d using the modified method from Shekhawat et al. To recreate this shift, the points of Lattice 1, Lattice 2, and the DSC lattice in the region between the two gray lines are all shifted by a DSC lattice vector oriented vertically, parallel to the grain boundary and perpendicular to the gray lines. This shift vector is shown by the small black arrow below the lower gray line. This nucleates oppositely oriented dislocations in the DSC lattice centered at the symbol, Đ, and shown in the inset. The introduction of this shift to all points between the gray lines is equivalent to the introduction of two edge dislocations of opposite orientation in the DSC lattice. The DSC dislocations naturally cause the CSL points (red) in the shifted region to translate by a lattice

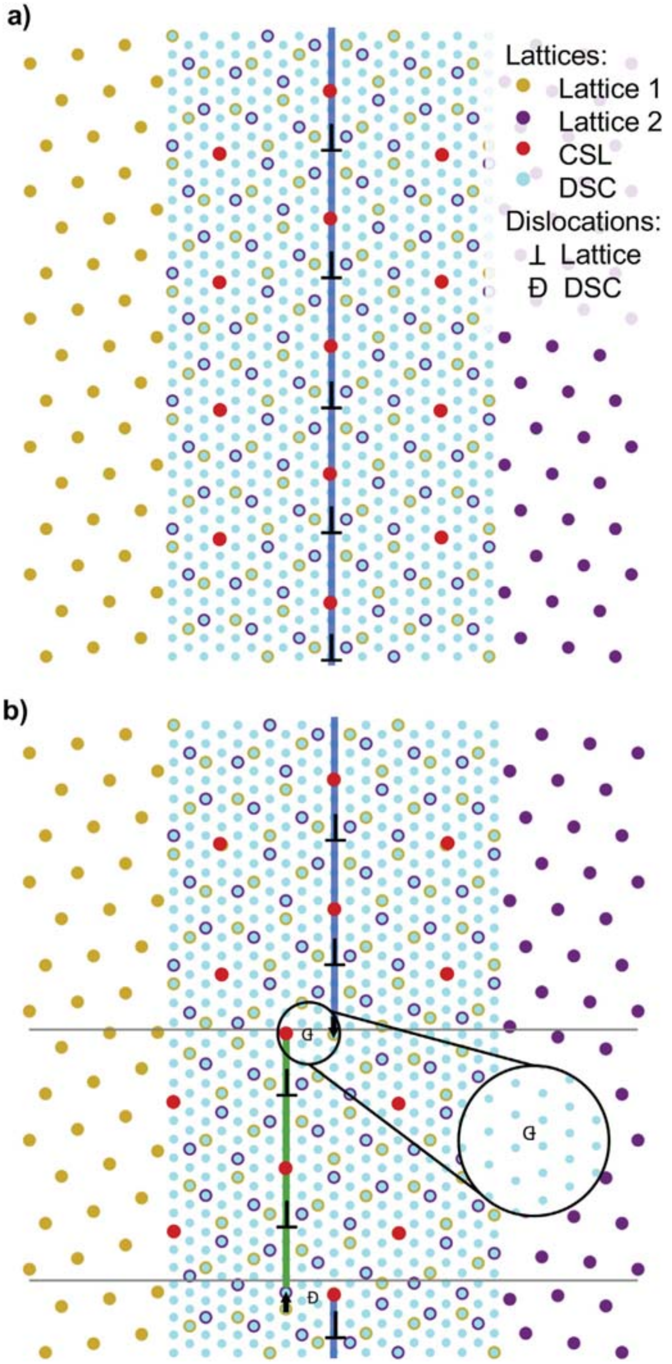

Fig. 2. Lattice representations of (a) straight and (b) kinked Σ7 grain boundaries display the equivalence of a grain boundary kink and a dislocation in the displacement shift complete (DSC) lattice. The two lattices are shown in gold and purple and are extended past the boundary (blue/green) to show the CSL lattice. Red points indicate the CSL, which represents the lattice points shared by both grains. Teal points indicate the DSC lattice, constructed so that it contains all points of both lattices. In (b), kinks in the grain boundary corresponds to a region (between the gray lines) where the CSL is shifted. The shift in the CSL can also be understood as dislocations in the DSC lattice, with the Burgers vector of the dislocation indicated by the black arrows. The inset isolates the DSC lattice around the dislocation core where there is an extra half-line of DSC lattice points. (For interpretation of the references to color in this figure legend, the reader is referred to the Web version of this article.)

vector of either Lattice 1 or 2 (and notably not by the DSC vector that describes the shifts of Lattice 1, Lattice 2, and the DSC lattice). We use the equivalent motion of the CSL points in both frames to create a topological connection between the atomistic and DSC representations of grain boundary migration. The shift in the CSL point caused by a DSC dislocation is the same as that associated with a grain boundary kink, and therefore effectively represents the presence of a kink in the grain boundary although there is no manifestation of the grain boundary in the DSC frame.

3. Simulation methods

3.1. Atomistic simulation

Before describing the details of our continuum formulation to predict grain boundary migration barriers, we first describe the atomistic simulations that we will use to validate the continuum approach. Computational supercells of varying height $\overline{H}$ and width W are created, each containing two anti-aligned grain boundaries with sigma number Σ separated by $W/2$, as shown in Fig. 1a. Due to the use of periodic boundary conditions, this amounts to modeling an infinite array of parallel grain boundaries of alternating direction. Total energies of atomic configurations are determined using LAMMPS [21]; we use the Tersoff functional with parameters found by Broido et al. to describe interactions between carbon atoms [22,23]. The atomic coordinates during minimization are constrained to be flat since we are most concerned with grain boundaries migration during annealing and in multilayer devices. In both of these cases, graphene remains flat and does not buckle out of plane. Therefore, we do not include the screening of elastic interactions due to out of plane buckling [12].

Grain boundary migration is represented by the process of kink nucleation and propagation, *i.e.* the glide of one 5–7 ring by one Burgers vector in each grain boundary and subsequent glide of adjacent dislocations. Each glide event results in the rearrangement of each atom's neighbors and creates a different topology (bonding network) within the supercell. As the kink propagates, the energy of each metastable state is determined by relaxing the structure while maintaining the bonding network. The energy barriers between the metastable states are ignored as we expect them to be independent with respect to grain boundary length H and, therefore negligible, relative to the total energy, in the large grain size limit [17]. In this way, the energy required to nucleate and propagate a kink in the supercell by one dislocation burgers vector is tracked.

Since our atomistic simulations invoke periodic boundary conditions, the energy of kink formation and propagation may be influenced by image interactions from neighboring supercells. To assess the magnitude of finite size effects, we present the effect of supercell parameters (W, $\overline{H}$) on the energy profile for a $\Sigma7$ boundary. Fig. 3a and b considers how the grain boundary migration barrier varies for different W for fixed $\overline{H} = 6$, and Fig. 3c and d considers how the grain boundary migration barrier varies for different $\overline{H}$ for fixed $W = 180$ Å. The energy profiles in Fig. 3a,c shows the nucleation and propagation of a grain boundary kink. The kink energy is shown *vs.* $\overline{K}/\overline{H}$ relative to that of the unkinked grain boundaries at $\overline{K}/\overline{H} = 0$. The migration energy is symmetric across the position $\overline{K}/\overline{H} = 0.5$ due to the periodic boundary conditions and translational symmetry of the grain boundaries. The maximum energy occurs at $\overline{K}/\overline{H} = 0.5$, which corresponds to the point where exactly half of the grain boundary has migrated. This energy is classified as the *barrier energy* for grain boundary motion. From the perspective of the DSC lattice, $\overline{K}/\overline{H} = 0$ and $\overline{K}/\overline{H} = 1$ correspond to the case where the two oppositely-oriented DSC dislocations for each grain boundary lie directly atop each other causing them to destructively interfere, whereas $\overline{K}/\overline{H} = 0.5$ corresponds to the case where the two DSC dislocations are maximally separated by $\overline{H}/2$.

Fig. 3a and b shows how the kink energy and the barrier height vary for different W and, therefore, the grain boundary spacing. The results show that beyond a cell width of ~100 Å, the kink energy plateaus and becomes insensitive to W. The corresponding analysis for the cell height $\overline{H}$ is shown in Fig. 3c and d. Instead of a plateau, the kink energy profiles increase monotonically with $\overline{H}$. The dependence of the barrier energy exhibits a logarithmic dependence on H, as shown by plotting the migration barrier for each in Fig. 3d. This is expected since grain boundary kinks are topologically equivalent to DSC dislocations, and dislocation interaction energies exhibit a logarithmic dependence on their spacing [24]. The logarithmic dependence of the barrier energy on the cell height and the plateau of barrier energy with cell width shows that the interaction energy of kinks from the same grain boundary is the dominant energy contribution for sufficiently large W such that the interaction with neighboring grain boundaries is minimized. Having established the nature of finite size effects in our simulations, all subsequent energy profiles are produced for supercells with $W, \overline{H}$ so that the intra-grain boundary kink energy is dominant according to the analysis of Fig. 3.

Next, we consider the dependence of kink energy on grain boundaries with varying Σ. Fig. 4a and b shows the kink energy *vs.* $\overline{K}/\overline{H}$ for various Σ boundaries with $W = 120$ Å and $\overline{H} = 10$. In the atomistic model, we use constant $\overline{H}$ as opposed to H because the periodicity of the boundary, a_{CSL}, does not allow for a constant H across Σ because a_{CSL} for each boundary is an irrational number making the least common multiple the product of a_{CSL} from each boundary. The energy profiles for high and low Σ are shown separately in Fig. 4a and b due to the two orders of magnitude difference in kink energies; note that the y-axis in Fig. 4b is scaled by a factor of 10^{-1}. Fig. 4c compares the energy barrier for each of the boundaries shown in Fig. 4a and b. We observe an empirical power-law relationship in which the migration barrier scales as $\sim \Sigma^{-0.95}$. Low Σ boundaries have a higher migration barrier and are less mobile, while high Σ boundaries have a lower, nearly negligible migration barrier and are more mobile.

To show that this trend persists even when comparing across constant H rather than constant $\overline{H}$, the inset in Fig. 4c shows the barrier height plotted *vs.* Σ for $H = 270$ Å (the cell height of the $\Sigma127$ boundary). The results in the inset are obtained *via* the continuum approach that will be described in the next section rather than atomistic simulation. The power law dependence remains, although each DSC energy calculated in the inset is slightly higher than its corresponding value in Fig. 4c. This is expected due to the logarithmic relationship of the barrier with H shown in Fig. 3d, which is represented by a larger exponent for the power fit $\sim \Sigma^{-1.07}$. The higher migration barrier for low Σ ($\Sigma7$, $\Sigma13$) boundaries is related to the observation that those boundaries are most commonly seen after CVD growth [8], while other boundary angles anneal from the system [9,13]. Using this understanding, coupled with the knowledge that dislocations anneal by merging with oppositely oriented dislocations, we posit that high Σ grain boundaries migrate and interact with low Σ grain boundaries. If they have opposite sign, their dislocations can annihilate or, if they are of the same sign, the boundaries merge until their dislocations are adjacent and form a near $\Sigma13$ structure although not necessarily with $\theta_l = 0$ [8,9].

3.2. Continuum model

We now develop a continuum formulation to capture the atomistic trends shown in Figs. 3 and 4 using a description of the

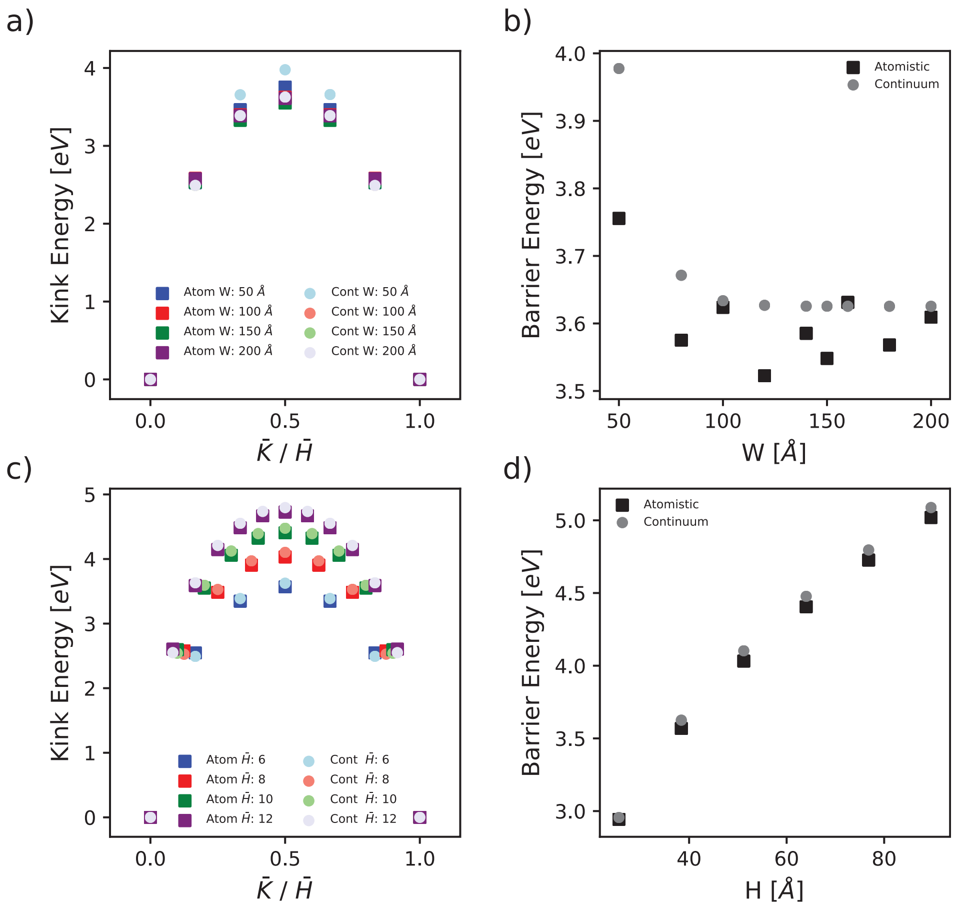

Fig. 3. The effect of simulation cell size on the migration energy for the Σ7 boundary. Squares represent atomistic results and dots continuum results. (a, b) The effect of changing the supercell width W at constant $\overline{H} = 6$ CSL periods. (a) The full energy profile for four different W are given. The maximum energy, defined here as the migration barrier, occurs at $\overline{K}/\overline{H} = 0.5$ corresponding to migrating half of the grain boundary. (b) The migration barrier energy is shown as a function of W. For $W > 100$ Å the barrier energy becomes relatively insensitive to W. (c) The effect of changing the supercell height, reported as the number of CSL periods $\overline{H}$, for constant at $W = 180$ Å on the full energy profile, and (d) the migration barrier energy for varying H showing a logarithmic dependence.

kinked grain boundaries as dislocations in the DSC lattice. Instead of explicitly considering the grain boundaries, we consider only the kinks in the grain boundaries, which we have shown to be equivalent to DSC dislocations. For each double kinked boundary, there are two oppositely oriented DSC dislocations located a distance $\overline{K}$ apart (a DSC dislocation dipole). Each supercell, containing two double-kinked grain boundaries, therefore contains a DSC dislocation quadrupole. For a given configuration, the spacing of the DSC dislocations in the quadrupole depends on $\overline{H}$, W, and $\overline{K}$. Since dislocation strain fields are long-ranged, dislocation-dislocation image interactions are present in these systems, and as shown above in Fig. 3, the energy of the quadrupole is sensitive to the supercell dimensions.

To find the energy associated with the presence of the DSC dislocation quadrupole, we use a continuum formulation for the energy of a set of dislocations in a linear elastic medium that naturally incorporates periodic boundary conditions and accounts for dislocation-dislocation interactions [25]. In this formulation, each dislocation introduces a topological constraint to the continuum distortion field Δ given by

$$\varepsilon_{kl}\partial_k \Delta_{lm} = \alpha_m \tag{1}$$

where $\Delta_{ij} = u_{i,j}$ is the ij -component of the distortion tensor and u_i is the i-component of the displacement field introduced by the DSC dislocations. The constraint states that the curl of the distortion field is equal to the Nye tensor (α), which gives the density of dislocations. For instance, the Nye tensor component α_m for a dislocation centered at the origin is given by

$$\alpha_k(\vec{r}) = b_k \delta(\vec{r}) \tag{2}$$

where b_k is the k component of the dislocations Burgers vector and δ the Kronecker-delta function. However, the singularity of the delta function in Eq. (2) is sufficient to cause the total energy of the dislocation to diverge. The divergence can be avoided by instead smearing the delta function into a gaussian according to

$$\alpha_k(\vec{r}) = b_k \exp\left(-\frac{\vec{r}^{\,2}}{R_{DSC}^2}\right), \tag{3}$$

where the parameter R_{DSC} is the gaussian width and defined as the DSC dislocation core radius; it is the single adjustable parameter of our model.

To account for the periodic boundary conditions and the resulting image interactions between dislocations in neighboring supercells, we write the distortion tensor as a sum over Fourier components $\tilde{\Delta}$ according to

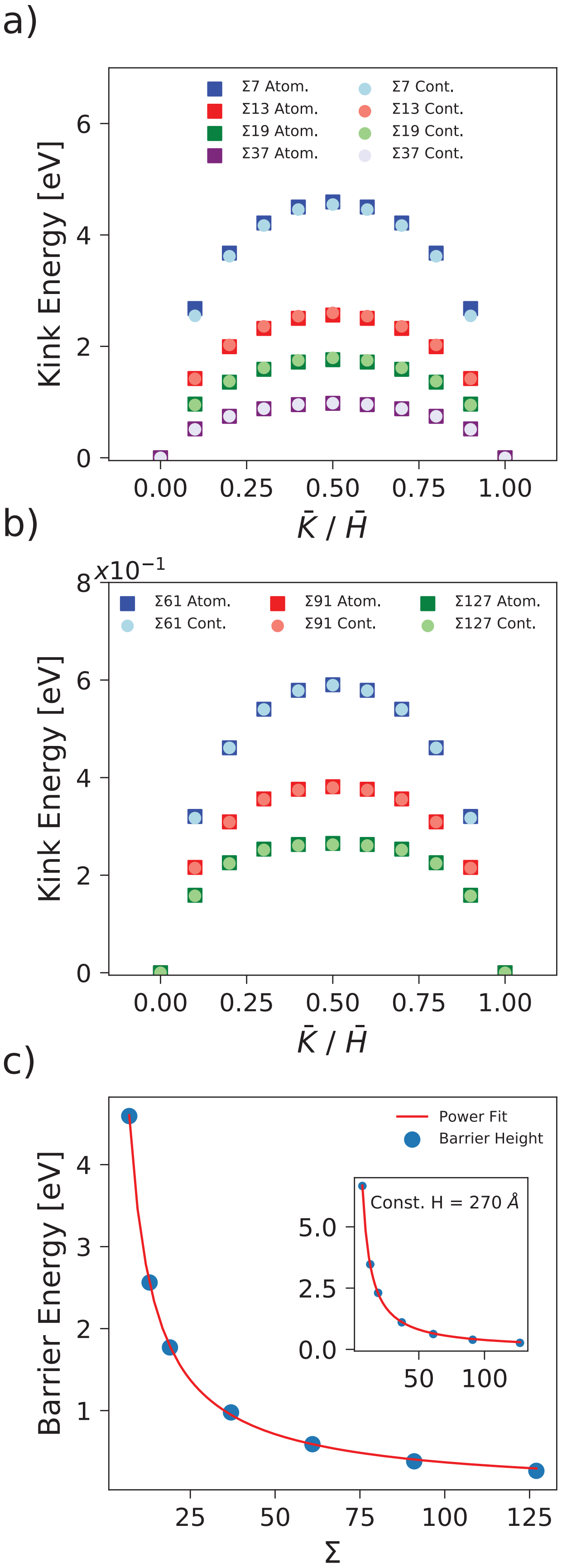

Fig. 4. Grain boundary migration energy profiles for various Σ with $W = 120$ Å, $\overline{H} = 10$ CSL periods. Squares represent atomistic results and dots continuum results. (a, b) Energy *vs.* $\overline{K}/\overline{H}$, the ratio of the grain boundary moved, for seven different Σ. (c) The atomistic grain boundary migration barrier energies show a $\sim\Sigma^{-1}$ power-law dependence for constant $\overline{H}$. The inset shows the barrier energies for constant $H = 270$ Å calculated with the continuum theory. The two cases exhibit the same scaling, although the barrier energies are slightly larger for the inset (due to larger H).

$$\Delta_{ij}\left(\vec{X}\right) = \sum_{\vec{G}} \tilde{\Delta}_{ij}\left(\vec{G}\right) \exp\left[i\vec{G}\cdot\vec{X}\right] \tag{4}$$

where $\vec{G}$ represents the reciprocal lattice (wave) vectors. The total distortion energy E_d associated with the distortion field is then given by

$$\begin{aligned} E_d &= \frac{1}{2} C_{jklm} \int\limits_{cell} \Delta_{jk} \Delta^*_{lm} dA \\ &= \frac{1}{2} \Omega_c C_{jklm} \sum_{\vec{G}} \tilde{\Delta}_{jk} \tilde{\Delta}^*_{lm} \end{aligned} \tag{5}$$

where C_{jklm} are the components of the fourth order elastic stiffness tensor as determined by the interatomic potential, and Ω_c is the supercell area.

By substituting Eqs. (3) and (4) into Eq. (1), a linear set of equations relating the Fourier components $\tilde{\Delta}$ for each $\vec{G}$ is obtained. However, the topological constraints of Eq. (1) do not uniquely determine the distortion tensor. The actual distortion field is the one that satisfies all topological constraints but uses all remaining degrees of freedom to minimize the total distortion energy in Eq. (5). The energy can be minimized separately for each $\vec{G}$ component as they are linearly independent. Once the components $\tilde{\Delta}$ are obtained, the energy terms are summed to find the total distortion energy. This approach has been applied previously to describe the energetics of 5–7 (real space) dislocations in two-dimensional materials [26], but to our knowledge this is the first application to dislocations in the DSC lattice to describe grain boundary kinks.

The best-fit core radius, R_{DSC} for the DSC dislocations is determined independently for each type of grain boundary Σ considered, *via* a least squares fit of the continuum model to all atomistic results sampling across different $\overline{H}$, W, and $\overline{K}$. The continuum results in Figs. 3 and 4a and b, use the best fit R_{DSC} for each Σ. The continuum approach captures all the trends of the atomistic simulations over the full range of Σ values and supercell dimensions, reproducing the migration energy profiles and barriers. For all cases considered, the maximum discrepancy between the continuum and atomistic framework is always less than 2%. The agreement between the atomistic and continuum curves show that, in essence, grain boundary kinks interact with each other elastically in a manner analogous to the interactions of linear elastic dislocations in the real crystal lattice.

4. Implications of DSC results

Since grain boundary kinks can be interpreted as DSC dislocations, we reinterpret the atomistic results with our continuum framework and dislocation theory. Fig. 5 shows the best-fit core radius normalized by the DSC dislocation Burgers vector $R_s = R_{DSC}/a_{DSC}$ as a function of Σ, revealing a linear relationship. The ratio between the CSL and DSC lattice vectors is also linear with Σ (*i.e.* $a_{CSL} = \Sigma\, a_{DSC}$), so the ratio of the core radius to the CSL lattice vector is constant across Σ. We believe this to be a general result for

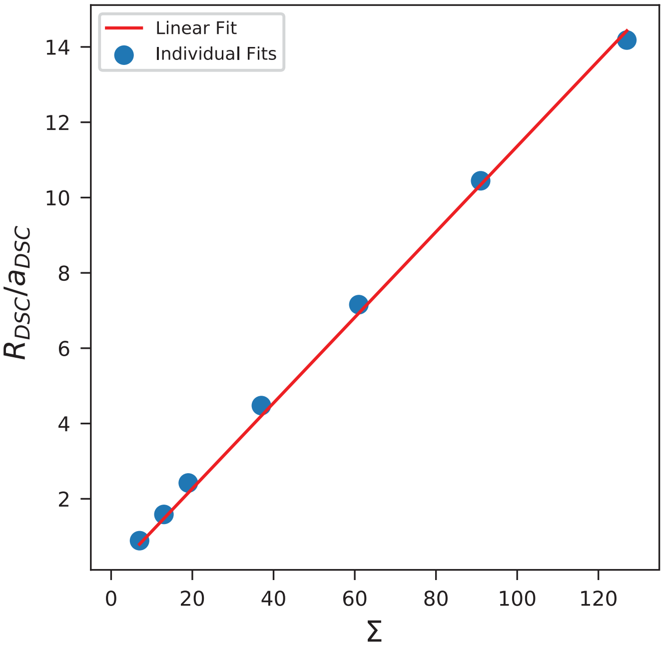

Fig. 5. The ratio R_{DSC}/a_{DSC} exhibits a near-linear dependence on Σ. Since a_{CSL} itself has a linear dependence on Σ, the ratio R_{DSC}/a_{CSL} is constant across all grain boundaries in graphene.

boundaries described using CSL/DSC theory because the normalization parameter a_{CSL} is a topological descriptor of the system. Rather than one core radius for each type of grain boundary, only one parameter, the slope of Fig. 5, is sufficient to define all core radii and, ultimately, the energetics of all grain boundary kinks in graphene. Numerically, for a given Σ boundary in graphene we obtain $R_{DSC} = 0.11\,\Sigma\,a_{DSC} = 0.11\,a_{CSL}$, where 0.11 is the slope in Fig. 5.

We return to Fig. 4c to analyze the $\sim\Sigma^{-1}$ power-law dependence of the migration barriers in light of the findings above. According to linear elasticity theory, the total energy of a dislocation scales as $b^2\ln(R_{disl}/R_{core})$, the square of the magnitude of the burgers vector multiplied by the natural log of the ratio of the dislocation spacing to the dislocation core radius [24]. The Burgers vector of DSC dislocations is given by the DSC lattice spacing, which scales according to $\Sigma^{-1/2}$ so $b^2\sim\Sigma^{-1}$. For the case of constant $\overline{H}$, as in the main part of Fig. 4c, we have $R_{disl}\sim\Sigma^{1/2}$ and $R_{core}\sim\Sigma^{1/2}$. This makes the term inside the logarithm a constant, resulting in an overall scaling of Σ^{-1} for the migration barrier, in good agreement with the numerically fitted value.

For the case of constant H, as in the inset of Fig. 4c, we still have $R_{core}\sim\Sigma^{1/2}$, but the dislocation–dislocation spacing R_{disl} is constant. This yields a migration barrier that scales as $-(1/2)\Sigma^{-1}\ln(\Sigma)$, and a corresponding difference between the curve in the inset and the main plot of Fig. 4c that scales as $\ln(\Sigma_\circ/\Sigma)$, where $\Sigma_\circ$ is the reference value of Σ (here $\Sigma_\circ = 127$). This shifts the barriers slightly upwards for the other $\Sigma > \Sigma_\circ$, and is responsible for the slightly higher magnitude exponent in the inset power-fit compared to the main plot. The numerical change of exponent on Σ is small because the variation of $\Sigma_\circ/\Sigma$ is within an order of magnitude throughout the considered domain. The scaling analysis of the power-fit from Fig. 4c further shows the ability of DSC dislocations to be described by the standard, linear elastic interaction energy of dislocations and supplements the correspondence between graphene grain boundary kinks and dislocations in the DSC lattice.

In conclusion, we have shown that grain boundary kinks in graphene are equivalent to DSC dislocations, which allows us to understand grain boundary structure and migration barriers using the linear elastic theory of dislocations. Our atomistic simulations show that grain boundary migration barriers have an inverse power-law dependence with Σ, which is attributed to the dependence of the DSC dislocation Burgers vector on Σ. We posit that the lower energy barrier of high Σ boundaries explains why they are not observed experimentally. The continuum analysis is unified across all boundaries by showing that the single fitting parameter, R_{DSC}, scales linearly with the CSL spacing. Together, these results provide examples of the usefulness of the DSC lattice to analyze the structure and motion of grain boundaries in graphene.

Acknowledgements

EA and EE acknowledge support through the National Science Foundation under Grants No. DMR-1555278 and DMR-1720633. EA and HTJ acknowledge support through ARO grant number ARMY W911NF-17-1-0544.

References

[1] Y. Wu, Y.-m. Lin, A.A. Bol, K.A. Jenkins, F. Xia, D.B. Farmer, Y. Zhu, P. Avouris, High-frequency, scaled graphene transistors on diamond-like carbon, Nature 472 (2011) 74 (EP –).
[2] L. Britnell, R.V. Gorbachev, R. Jalil, B.D. Belle, F. Schedin, A. Mishchenko, T. Georgiou, M.I. Katsnelson, L. Eaves, S.V. Morozov, N.M.R. Peres, J. Leist, A.K. Geim, K.S. Novoselov, L.A. Ponomarenko, Field-effect tunneling transistor based on vertical graphene heterostructures, Science 335 (2012) 947–950.
[3] D. Chong-an, W. Dacheng, Y. Gui, L. Yunqi, G. Yunlong, Z. Daoben, Patterned graphene as source/drain electrodes for bottom-contact organic field-effect transistors, Adv. Mater. 20 (2008) 3289–3293.
[4] Y. Li, X. Fan, J. Qi, J. Ji, S. Wang, G. Zhang, F. Zhang, Gold nano-particlesÃćÂĂÂŞgraphene hybrids as active catalysts for suzuki reaction, Mater. Res. Bull. 45 (2010) 1413–1418.
[5] H. Yi, X. Zhen, G. Chao, Ultrathin graphene nanofiltration membrane for water purification, Adv. Funct. Mater. 23 (2013) 3693–3700.
[6] A. Bonanni, M. Pumera, Graphene platform for hairpin-dna-based impedimetric genosensing, ACS Nano 5 (2011) 2356–2361.
[7] F. Schedin, A.K. Geim, S.V. Morozov, E.W. Hill, P. Blake, M.I. Katsnelson, K.S. Novoselov, Detection of individual gas molecules adsorbed on graphene, Nat. Mater. 6 (2007) 652 (EP –).
[8] C. Ophus, A. Shekhawat, H. Rasool, A. Zettl, Large-scale experimental and theoretical study of graphene grain boundary structures, Phys. Rev. B 92 (2015) 205402.
[9] A.V. Tyurnina, H. Okuno, P. Pochet, J. Dijon, Cvd graphene recrystallization as a new route to tune graphene structure and properties, Carbon 102 (2016) 499–505.
[10] Y. Wei, J. Wu, H. Yin, X. Shi, R. Yang, M. Dresselhaus, The nature of strength enhancement and weakening by pentagon–heptagon defects in graphene, Nat. Mater. 11 (2012) 759 (EP –).
[11] A.W. Tsen, L. Brown, M.P. Levendorf, F. Ghahari, P.Y. Huang, R.W. Havener, C.S. Ruiz-Vargas, D.A. Muller, P. Kim, J. Park, Tailoring electrical transport across grain boundaries in polycrystalline graphene, Science 336 (2012) 1143–1146.
[12] O.V. Yazyev, S.G. Louie, Topological defects in graphene: dislocations and grain boundaries, Phys. Rev. B 81 (2010) 195420.
[13] J. Zhuang, R. Zhao, J. Dong, T. Yan, F. Ding, Evolution of domains and grain boundaries in graphene: a kinetic Monte Carlo simulation, Phys. Chem. Chem. Phys. 18 (2016) 2932–2939.
[14] A. Shekhawat, C. Ophus, R.O. Ritchie, A generalized read-shockley model and large scale simulations for the energy and structure of graphene grain boundaries, RSC Adv. 6 (2016) 44489–44497.
[15] M. Guillope, J. Poirier, A model for stress-induced migration of tilt grain boundaries in crystals of nacl structure, Acta Metall. 28 (1980) 163–167.
[16] H. Khater, A. Serra, R. Pond, J. Hirth, The disconnection mechanism of coupled migration and shear at grain boundaries, Acta Mater. 60 (2012) 2007–2020.
[17] A. Rajabzadeh, F. Mompiou, M. Legros, N. Combe, Elementary mechanisms of shear-coupled grain boundary migration, Phys. Rev. Lett. 110 (2013) 265507.
[18] W.T. Reynolds, Interfaces in Crystalline Materials by A. P. Sutton, (University of Oxford) and R. W. Balluffi (MIT). Oxford University Press, New York, 1995 xxvii + 819 pp. $165. ISBN 0-19-851385-2., volume 119, American Chemical Society, 1997.
[19] D. Warrington, P. Bufalini, The coincidence site lattice and grain boundaries, Scripta Metall. 5 (1971) 771–776.
[20] D.H. Warrington, The coincidence site lattice (csl) and grain boundary (dsc) dislocations for the hexagonal lattice, J. Phys. Colloq. 36 (1975). C4–C87–C4–95.

[21] http://lammps.sandia.gov.

[22] S. Plimpton, Fast parallel algorithms for short-range molecular dynamics, J. Comput. Phys. 117 (1995) 1–19.

[23] L. Lindsay, D.A. Broido, Optimized tersoff and brenner empirical potential parameters for lattice dynamics and phonon thermal transport in carbon nanotubes and graphene, Phys. Rev. B 81 (2010) 205441.

[24] J. Hirth, J. Lothe, Theory of Dislocations, Krieger Publishing Company, Malabar, Florida, 1992.

[25] M.S. Daw, Elasticity effects in electronic structure calculations with periodic boundary conditions, Comput. Mater. Sci. 38 (2006) 293–297.

[26] E. Ertekin, D.C. Chrzan, M.S. Daw, Topological description of the stone-wales defect formation energy in carbon nanotubes and graphene, Phys. Rev. B 79 (2009) 155421.